

Valley Emission and Upconversion in Isotopically Engineered Monolayer WS₂ under Resonant Excitation

Rahul Kesarwani^{1,2}, Vaibhav Varade¹, Artur Slobodeniuk¹, Martin Kalbac^{2*}, and Jana Vejpravova^{1*}

¹ Department of Condensed Matter Physics, Faculty of Mathematics and Physics, Charles University, Ke Karlovu 5, 121 16 Prague 2, Czech Republic

² Department of Low-Dimensional Systems, J. Heyrovsky Institute of Physical Chemistry, Dolejskova 3, 182 23 Prague 8, Czech Republic

*Email: martin.kalbac@jh-inst.cas.cz

*Email: jana.vejpravova@matfyz.cuni.cz

Keywords: 2D materials, isotope engineering, resonant excitation, valley polarization, photoluminescence, upconversion, interband and intraband scattering.

Abstract

In the quest to optimize the optoelectronic and valleytronic properties of 2D materials, various strategies such as strain engineering, doping, and heterostructuring have been explored. In this direction, isotope engineering also offers a potential avenue to alter electron-phonon interaction and impact quasiparticle scattering processes. In this study, we investigate the dependence of sulfur isotopes on upconversion and valley scattering phenomena by collecting the resonance photoluminescence (PL) under an applied magnetic field from 0 to 14 T at 4 K for the chemical vapor deposition-grown monolayer (1L) of W^NS₂, W³²S₂, and W³⁴S₂. The upconversion of the mixed-state sulfur 1L (W^NS₂) exhibits one *M*-phonon absorption, with an obtained optical gain of nearly 30 meV, while the pure sulfur isotope labelled 1Ls (W³²S₂ and W³⁴S₂) require two phonons (*M* and *Γ*), yielding a gain of around 80 meV. It is also found that the exciton degree of polarization (DOP) of W^NS₂ changes significantly by ~ -30% as the field increases from 0 to 14 T, while for W³²S₂ and W³⁴S₂, the exciton DOP increases by up to ~8%. Similarly, distinct changes in the DOP are observed for trions and localized excitons among all the samples, attributed to the different valley scattering phenomena. The 1L W^NS₂ demonstrates a combination of intraband and interband scattering, whereas in the case of W³²S₂ intraband scattering is preferred; W³⁴S₂ predominantly exhibits interband scattering. Finally, a phenomenological model is proposed to describe the upconversion and valley scattering processes.

1. Introduction

Two-dimensional (2D) transition metal dichalcogenide (TMD) materials have emerged as promising platforms for various concepts for optics, sensing, and nanoelectronics [1–3]. Recently, upconversion phenomena have been reported as a promising approach to boost the opto-electronic properties of TMDs, wherein lower-energy photons are efficiently converted into higher-energy ones [4,5]. By converting lower-energy photons into higher-energy ones, upconversion transitions enhance the overall efficiency of light emission, which is advantageous for applications such as solar cells, light-emitting diodes, optoelectronic devices, and optical refrigeration in semiconductors [6–9]. Upconversion mechanisms, including excited state absorption, sequential energy transfer, cooperative transitions, and photon avalanche, are governed by distinct electronic interactions. Among these, energy transfer and excited state absorption dominate due to their higher efficiencies, especially in sensitizer–activator systems [10]. Understanding stepwise electronic excitation, phonon-assisted energy transfer, and non-radiative relaxation is crucial for optimizing upconversion materials. Leveraging the unique properties of 2D-TMD materials, including their atomically thin nature (enabling enhanced quantum confinement and reduced dielectric screening) and tunable electronic structure (facilitating direct-to-indirect bandgap transitions and strong excitonic effects), various mechanisms have been proposed, including electron-electron, electron-phonon, exciton-phonon, and phonon-phonon interaction processes, potentially influencing parameters such as the degree of polarization (DOP), intra/interband scattering, binding exciton energy, trion-to-exciton ratios, and localized exciton states [5,11–15]. Understanding and optimizing these processes is crucial for enhancing the efficiency and applicability of upconversion in 2D-TMD materials.

Furthermore, upconversion transitions enable the detection of weak signals by amplifying them through the accumulation of photons during the absorption process. This heightened sensitivity is invaluable for various sensing and imaging applications, including biological sensing and environmental temperature monitoring [16,17]. In monolayer (1L) TMDs, this phenomenon can lead to unique optical properties and novel applications, such as nonlinear optics and quantum information processing [18–20]. More significantly, photoluminescence (PL) in 1L TMDs can potentially be regulated by isotope engineering (IE) (substituting transition metal (TM) and sulfur (S) isotopes), electrical doping, charge transfer through heterostructures, structural light, etc. [21–

26]. This alteration can further impact the properties of electron states in the crystal, leading to the modification of the electronic band structures, resulting in the modification of the exciton masses and binding energies [27,28]. Furthermore, Wu et al. [29] and Vuong et al. [30], respectively, discussed the theoretical influence of tungsten (W) isotopes and experimentally exhibited the effect of boron (B') isotopes on spin-dependent properties and intra/interband transitions/scattering in both K^+ and K^- valleys. Such isotopic effects offer a novel opportunity for tuning 2D materials' physical properties while maintaining an identical chemical composition. Likewise, the isotopic effect of S on optical properties in TMDs has been minimally explored. Early discussions by Varade et al. [31] emphasized the S isotopic effect on the optical properties (Raman and PL) of 1L MoS₂ under non-resonance excitation, showing the fundamental role of S isotopes in the phonon-driven properties of MoS₂.

Understanding the impact of S isotopes on upconversion phenomena under resonance conditions could complete the picture of valley scattering processes. Earlier studies have focused on oxide isotope precursors and magnetic field effects, while S isotopes may offer additional insights into these dynamics. Although reports on the effect of magnetic field on resonance PL in 1L TMDs are limited, it is well-established that magnetic fields enhance quasiparticle scattering between the K^+ and K^- valleys [32–34]. However, similar scattering processes have not been widely discussed for other material systems beyond 2D TMDs. Therefore, further comprehensive investigations are required to analyze the isotopic effects of S on the Raman and PL properties, under resonance excitation by varying magnetic fields and temperatures, of 1L TMDs.

Over the past decade, researchers have expanded the scope of IE to encompass graphene and various semiconductors [35,36]. While materials like WS₂ and MoS₂ primarily involve oxide isotope variations and hBN focuses on B' isotopes, detailed reports on IE in 2D materials remain limited [21,30,31,37–39]. The works predominantly focus on varying TM isotopes (W, Mo, and B') and their impact on transport properties, limiting the investigations of the optical properties, which are essential with respect to the most promising applications of TMDs. Additionally, it has been reported that the alteration of isotopes can modify both electron-phonon interactions and the exciton dynamics [40]. Despite generic claims of the minimal effects of the chalcogenide isotopes (S) on physical properties (both optical and transport), experimental and theoretical evidence remains inconclusive [29].

The present study investigates the isotopic effects of S in 1L WS₂, with a focus on PL under resonant excitation. The chemical vapor deposition (CVD) technique is employed to fabricate high-quality WS₂ monolayers incorporating natural S, ^NS (W^NS₂), and isotopically pure ³²S (W³²S₂) and ³⁴S (W³⁴S₂), recognized as the most stable and prevalent isotopes within the S isotopic spectrum. The polarization-resolved optical experiments are carried out down to cryogenic temperatures under magnetic fields ranging from 0 to 14 T. Our results stress a significant influence of IE on PL upconversion and make it possible to uncover the interband and intraband scattering mechanisms under the applied magnetic field. The study provides important insights into the intricate interplay of isotopic effects in valley-driven physics and upconversion processes in 1L TMDs.

2. Experimental Details

WS₂ 1Ls were grown on a silicon (Si) substrate covered with a 300-nm-thick layer of silicon oxide (SiO₂). The substrate was cleaned through subsequent sonication in deionized water, acetone, and isopropanol (Sigma-Aldrich). The fabrication of WS₂ took place in a quartz tube using a horizontal furnace with two heating zones, under atmospheric pressure, employing argon as the carrier gas. Initially, the tube was connected to an argon gas line at one end and to a bubbler filled with a 100 mM aqueous solution of KOH. The tube was flushed with argon at a continuous flow of 200 cm³ min⁻¹ at a temperature of ~105°C for 15 minutes. The precursor, WO₃ (155 mg) powder (Thermo Scientific—LOT: R04G047), was placed in the crucible at the first heating zone (high temperature), and the substrate was placed face-down on top of the crucible. Simultaneously, 100 mg of ^NS (Thermo Scientific—LOT: T29G013) was placed in a tube, 20 cm away, at the second heating zone (low temperature). Maintaining a constant argon flow rate of 150 cm³ min⁻¹, the temperature was subsequently increased in the tube at a constant rate of 40°C min⁻¹. When the temperature reached ~770°C in the first heating zone, the heating in the second zone was initiated. The temperatures were held constant at ~990°C in the first zone and ~220°C in the second zone for 10 minutes, after which the furnace was opened, and the system was allowed to cool ambiently. A similar process was adopted for the other two isotopes of sulfur to obtain 1Ls of W³²S₂ and W³⁴S₂.

Atomic force microscopy (AFM) images and thickness profiles were obtained using Bruker's AFM Dimension ICON system in the Peak Force Quantitative Nanomechanical Mapping mode

with a Bruker silicon tip. The AFM data were processed and analyzed by open-access Gwyddion software.

Micro-Raman and PL spectra were measured using an in-house spectroscopic setup that collects the signals in a backscattering geometry using a low-temperature confocal Raman microscope insert (attoRAMAN, attocube) placed in a Physical Property Measurement System (PPMS, Quantum Design). A low-temperature- and magnetic-field-compatible 100× objective (numerical aperture 0.82 and lateral resolution of 500 nm) lens was used to focus the resonance (633 nm or 1.96 eV) and non-resonance (532 nm or 2.33 eV) excitation with linear and circularly polarized light at a power of 100 μ W. The WITec spectrometer was used to scan the map of 1L flakes of size 20–30 μ m for PL and Raman spectra with a spatial resolution of 0.5 μ m using a grating of 600 and 1800 lines/mm, respectively. The incident laser beam was circularly polarized using a set of standard 633 nm half- and quarter-wave plates. Similarly, a series of broadband quarter- and half-wave plates were used to obtain polarization-resolved emitted signals. More details regarding the experimental setup are discussed in our previous paper [41].

3. Results and Discussion

Raman and PL Characterizations

We prepared samples of $W^N S_2$, $W^{32} S_2$, and $W^{34} S_2$ using CVD method from isotopically labeled precursors. AFM and Raman analysis confirm that the prepared WS_2 samples consist solely of monolayers. The AFM images and its thickness measurements are shown in Figure 1.

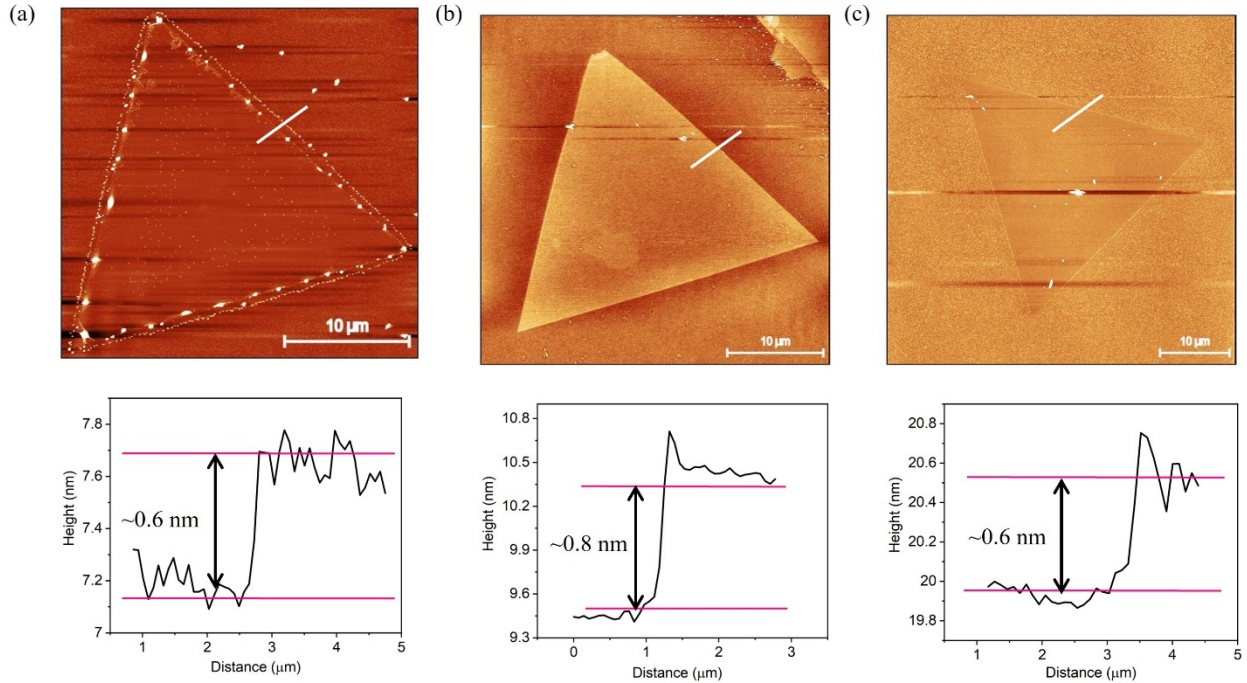


Figure 1. Surface morphology of isotope modified monolayers (1L) WS_2 . AFM analysis for surface profile and thickness measurement of 1-Ls. (a) $\text{W}^{\text{N}}\text{S}_2$, (b) W^{32}S_2 , and (c) W^{34}S_2 .

The Raman spectra of isotopically labeled WS_2 monolayers at 300 K (under non-resonant 532 nm, 2.33 eV excitation) are shown in Figure 2(a). We observe that the peak position of the $\text{A}_{1\text{g}}$ phonon mode remains nearly identical for $\text{W}^{\text{N}}\text{S}_2$ (mixture of S isotopes: ^{32}S (95%), ^{34}S (4.25%) and ^{33}S (0.75%)) and W^{32}S_2 , while it is redshifted in W^{34}S_2 (inset of Figure 2(a)). This redshift primarily results from the S isotope mass effect, where the heavier ^{34}S isotope leads to a decrease in phonon energy. The phonon frequency follows an inverse square root dependence on mass ($\omega \propto 1/\sqrt{m}$), leading to a systematic shift in the Raman-active modes of isotopically engineered materials [42]. Although strain and phonon dispersion variations can influence Raman shifts, the fewer shift between $\text{W}^{\text{N}}\text{S}_2$ and W^{32}S_2 suggests that isotope-induced mass changes are the dominant factor. The observed shift is consistent with previous reports on isotopically modified TMDs [31]. Figure 2(b) shows the deconvoluted Raman spectrum of W^{32}S_2 at 4 K (under excitation 633 nm, 1.96 eV). In this case, additional phonon modes are activated, and new bands are observed at 385 cm^{-1} , 355 cm^{-1} , 213 cm^{-1} , 171 cm^{-1} , and 145 cm^{-1} in addition to the $\text{A}_{1\text{g}}$ and $\text{E}_{2\text{g}}$ modes. The phonons of resonant modes can be responsible for upconversion and intra/interband phenomena (further details discussed below) [43]. Full deconvoluted Raman spectra measured at the resonance excitation of $\text{W}^{\text{N}}\text{S}_2$ and W^{34}S_2 are presented in Figure S1 (SI). The excitation energy is not expected to affect

the Raman peak positions. We indeed observed a similar difference in the shift of the A_{1g} phonon mode for the $W^N S_2$, $W^{32} S_2$, and $W^{34} S_2$ 1Ls (see Table S1 in SI), as in the case of non-resonance conditions. (The complete list of the resonance phonon peaks, along with their respective assignments for all the isotopes of modified WS_2 , is shown in Table S1 (SI).)

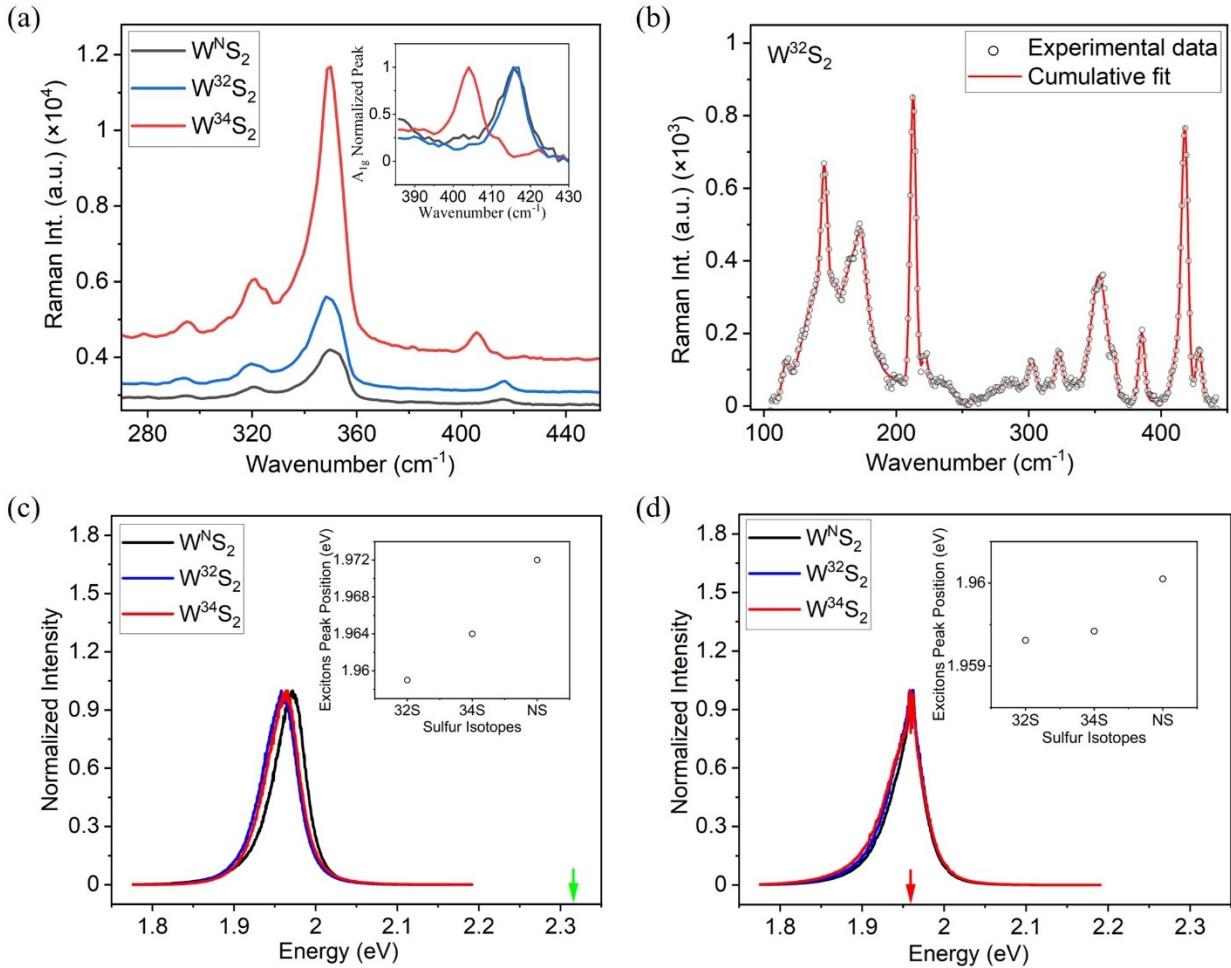


Figure 2. Raman/PL of the $W^N S_2$, $W^{32} S_2$, and $W^{34} S_2$ 1Ls: (a) Raman spectra at 300 K under non-resonance excitation. (b) Raman spectra at 4 K under resonance excitation. PL spectra at 300 K under (c) non-resonance and (d) resonance excitation. The arrow represents the excitation energy.

The PL spectra measured for $W^N S_2$, $W^{32} S_2$, and $W^{34} S_2$ at 300 K are shown in Figure 2(c) and (d) under non-resonance and resonance excitation, respectively. Upon initial inspection, the energy bandgap (or excitonic peak) of isotope-modified WS_2 for downconversion (non-resonance excitation, inset of Figure 2(c) shows a blueshift of ~ 4 meV with varying isotopes from ^{32}S to ^{34}S , as observed in conventional semiconductors due to the involvement of phonons in the indirect

band-to-band transition [30,44]. Further, the exciton energy is found to blueshift by ~ 7 meV in $W^N S_2$ with respect to $W^{32} S_2$, which can be attributed to isotope mixture-induced disorder. In contrast, in the case of upconversion (resonance excitation, inset of Figure 2(d)), the exciton energy shift due to different isotopes is negligible due to direct band-to-band transition, which does not involve phonons.

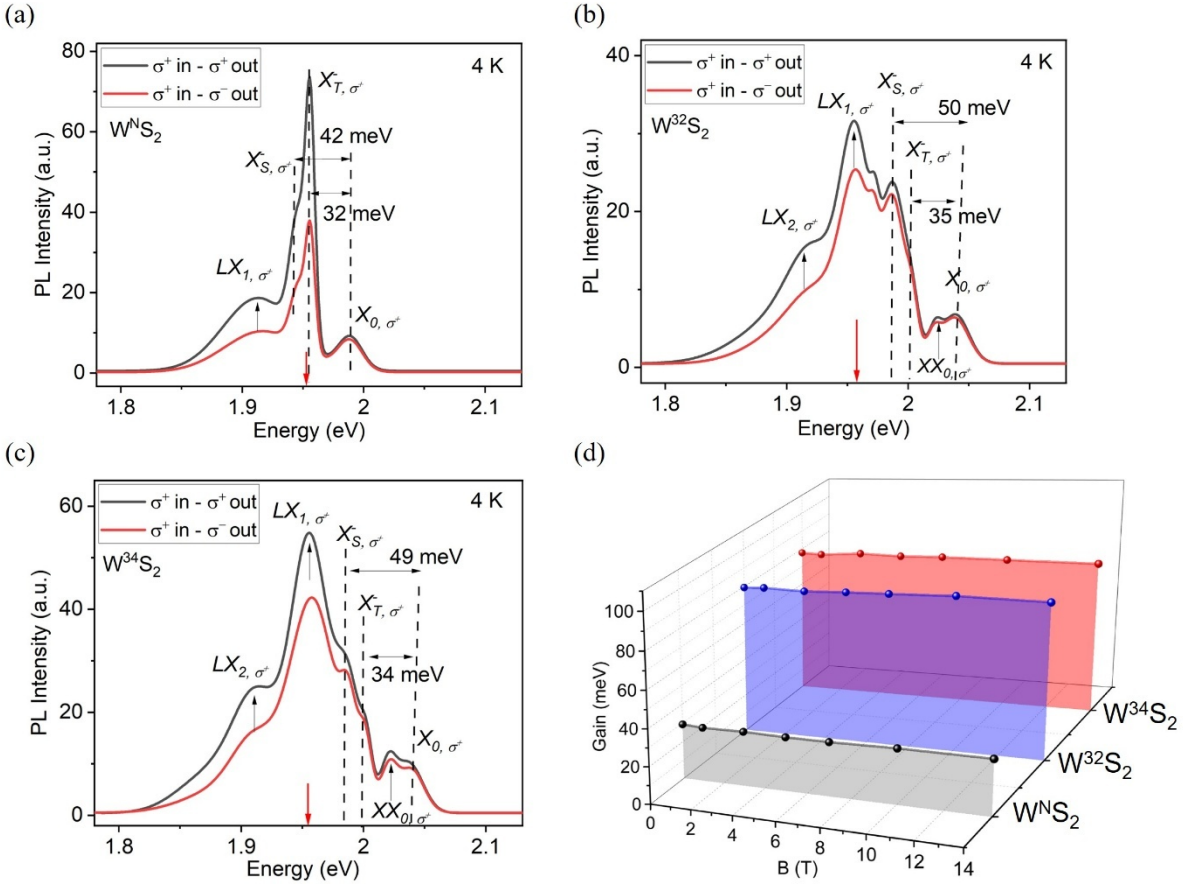


Figure 3. PL spectra of sulfur isotopes of modified WS_2 1Ls at 4 K and 0 T under resonance excitation: (a) $W^N S_2$, (b) $W^{32} S_2$, and (c) $W^{34} S_2$. The assigned peaks of exciton (X_{0,σ^+}), trions ($X_{i(=T,S),\sigma^+}^-$), and localized excitons ($LX_{i(=1,2),\sigma^+}$) are identified after the deconvoluted PL spectra of σ^+ excitation (“ σ^+ in”) and σ^+ detection (“ σ^+ out”), along with their binding energy. (d) Comparison of exciton gain among different isotopes is obtained using “ σ^+ out” polarization state depending on applied magnetic fields. The arrow indicates the excitation energy.

To probe the circular DOP and intra/interband scattering within/between K^+ and K^- valleys, we collected circularly polarized magneto-PL spectra at 4 K for the set of isotopically modified WS₂ 1Ls. The magneto-PL measurements are carried out with the excitation of right circularly polarized light, denoted as “ σ^+ in,” and the emission is detected in both the right and left circular polarization states, referred as “ σ^+ out” and “ σ^- out,” respectively, under varying magnetic fields from 0 to 14 T. Figure 3(a)–(c) shows the initial PL spectra of both “ σ^+ out” and “ σ^- out” for the 1Ls of W^NS₂, W³²S₂, and W³⁴S₂, respectively, recorded at 4 K at 0 T. The PL of 1L WS₂ is characterized by distinct quasiparticles, and their identified peak positions for “ σ^+ out” polarized light are shown. These PL bands are assigned as follows: “exciton” refers to “ X_{0,σ^+} ,” “biexciton” to “ XX_{0,σ^+} ,” “triplet trion” to “ X_{T,σ^+}^- ,” “singlet trion” to “ X_{S,σ^+}^- ,” and “localized excitons” to “ $LX_{i(=1,2),\sigma^+}$.” Notably, the characteristic PL spectra at 4 K of the 1Ls W³²S₂ and W³⁴S₂ exhibit two LX peaks and one neutral XX_0 peak, while the mixed-isotope 1L shows only one LX peak. The complete deconvoluted PL spectra of both the “ σ^+ out” and “ σ^- out” polarization states of all the isotopes of modified WS₂ measured at 4 K are shown in Figures S2 and S3 (in the SI). The peak positions obtained by deconvoluting the PL spectra are listed in Table S2 in the SI; for example, X_{0,σ^+} , X_{T,σ^+}^- , and LX_{1,σ^+} for W^NS₂ at 4 K and 0 T were found to be around 1.989 eV, 1.956 eV, and 1.913 eV, respectively, and they are in agreement with the previous reports on CVD-grown 1L WS₂ [5,12,45–47]. Spectral deconvolution of the PL spectra was carried out using Origin software, where each spectrum was fitted with Gaussian peaks to determine peak positions, area under the curve, and intensity ratios for various quasiparticles. The best fit was selected based on R^2 values (close to 1), ensuring an accurate and reliable decomposition of the spectra.

Importantly, S isotopes impact the optical properties of 1L WS₂, as evidenced by the characteristic PL spectra and estimated trion binding energies. The estimated binding energies ($E_{bX_{i(=T,S)}^-} = X_0 - X_{i(=T,S)}^-$) of X_{T,σ^+}^- and X_{S,σ^+}^- in W^NS₂ are 32 and 42 meV, respectively, which results in an energy difference (δ_{TS}) between X_{T,σ^+}^- and X_{S,σ^+}^- of 10 meV, consistent with previous reports [5,46,47], where the values were observed from 6 to 11 meV. However, in W³²S₂, the binding energies for X_{T,σ^+}^- and X_{S,σ^+}^- are 35 and 50 meV, respectively, resulting in $\delta_{TS} \sim 15$ meV. Similarly, for W³⁴S₂, the binding energies are nearly identical (34 and 49 meV) to W³²S₂, with the same δ_{TS} (displayed in Figure 3). δ_{TS} is found to increase slightly (2–3 meV) with varying magnetic fields (0 to 14 T) in the case of all the isotope-modified WS₂ 1Ls; see Table S2 in the SI. Some reports indicated that

δ_{TS} decreases if an hBN spacer is placed between WS₂ and the substrate [5,11]. Building upon this finding, the observed variations in both the PL characteristic and binding energies within isotope-modified WS₂ samples can be ascribed to a S lattice mismatch with the substrate lattice. In the case of the mixed state (W^NS₂), the S lattice mismatch is likely to be more pronounced, leading to reduced interaction with the substrate. Conversely, the pure isotope states of samples demonstrate a strong interaction with the local field of the SiO₂ substrate, resulting in the induction of a more localized band and thus increased δ_{TS} [11,48,49]. To further investigate the influence of substrate interactions and strain effects, we analyzed the correlation between the E_{2g} and A_{1g} Raman modes. The observed shifts provide insights into possible strain contributions, supporting the hypothesis of substrate-induced effects in the pure isotope samples. A correlation plot between the E_{2g} and A_{1g} Raman mode shifts is presented in Figure S4 (in SI).

To further verify the positions of the quasiparticle peaks in the case of isotopically pure samples, we analyzed the temperature dependence of PL for the “ σ^+ out” detection of 1L W³²S₂. The observed changes of peak shifts with temperature, as illustrated in Figure S5(a), align with previously reported behavior [45,50]. Additionally, the positions of excitons and trions versus temperature closely follow the Varshni model (Figure S5(b) and (c)), while localized excitons fit well with the Manoogian model (refer to Figure S5(d)) [31,51]. Furthermore, we analyzed the integral intensity ratio, $I_{X_{\sigma^+}^-}/I_{X_{0,\sigma^+}}$, of trions to excitons (Figure S5(e)); it shows that trions are more pronounced at low temperatures due to reduced thermal energy and phonon coupling effects [52]. Further, Figure S5(f) shows the intensities of quasiparticles at different temperatures following the usual trend in resonant excitation reported previously [51,53]. The power dependence of the intensity of excitonic peaks at 4 K and 300 K (Figure S5(g)) is found to follow a typical power law with an exponent value ~ 0.77 [50]. Moreover, the neutral XX₀ peak is observed only in the 1Ls W³²S₂ and W³⁴S₂. The peak assignment of XX₀ is confirmed by analyzing the ratio of the scaling factor between the assigned peak and the exciton peak intensity variation with excitation power. It was found that the scaling factor for the biexciton is twice that of the exciton, confirming that the assigned peak in our PL spectra corresponds to biexcitonic emissions (see Figure S5(h) in SI). This analysis also highlights the spectral variations between pure and mixed isotopes. Additionally, Figure S5(i) – (j) illustrates the variation of trion binding energy with excitation power, showing an increase at 300 K that stabilizes at higher power levels, while at 4 K, the variation remains minimal (1–2 meV), consistent with previous reports [26,54].

The optical gain G is defined as the difference between the incident light energy (1.962 eV) and exciton energy, X_0 ($G = 1.962 - X_0$). A positive value of G indicates upconversion phenomena, while a negative value denotes downconversion [55]. Upconversion phenomena have been observed for 2D materials under resonance excitation in earlier reports [5,12,13]. Figure 3(d) illustrates the optical gain obtained from measurement of the “ σ^+ out” PL signal for $W^N S_2$, $W^{32} S_2$, and $W^{34} S_2$, with the magnetic field being varied from 0 to 14 T. We observed that the optical gain for $W^N S_2$ is approximately 30 meV, while for $W^{32} S_2$ and $W^{34} S_2$, it is around 80 meV for a 0 T field and remains nearly constant as the magnetic field is increased to 14 T for all the measured samples. This can be explained by the fact that the Zeeman shift of exciton energies is an order of magnitude smaller (typically 2 meV per 10 T) than the observed shifts of tens of meV [56]. Additionally, the observed variation in optical gain among the samples likely arises from differences in excitonic interactions and phonon-mediated processes influenced by the isotope mass effect. Similar behavior has been observed for the “ σ^- out” detection polarization states of $W S_2$ 1Ls irrespective of their S isotopic composition, as shown in Figure S6 (SI).

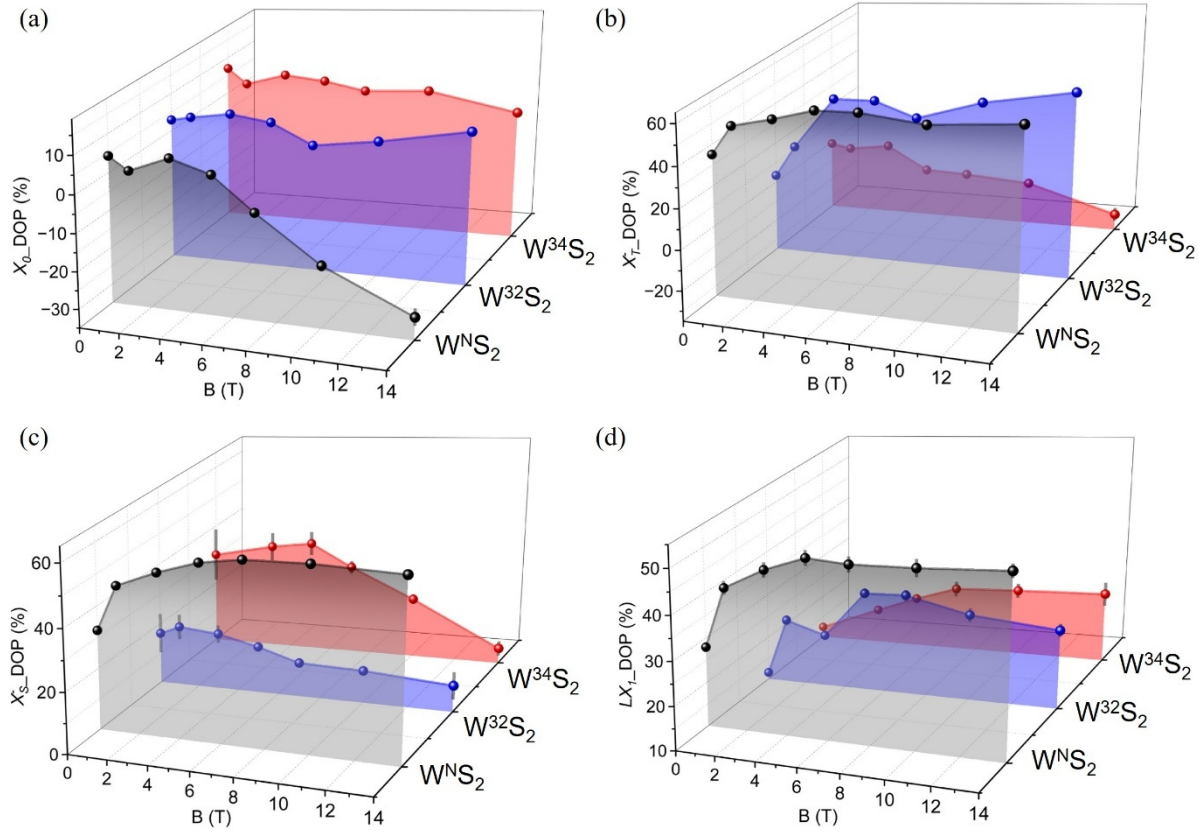


Figure 4. DOP of S isotopes of modified WS₂ 1L at 4 K under magnetic field: (a) Exciton (X_0), (b) triplet trion (X_T^-), (c) singlet trion (X_S^-), and (d) localized exciton (LX_1).

DOP and Intensity Ratios

The circular DOP is defined as $DOP = \frac{I_{\sigma^+} - I_{\sigma^-}}{I_{\sigma^+} + I_{\sigma^-}}$, where I_{σ^+} and I_{σ^-} represent the intensities of quasiparticles extracted from the deconvoluted PL spectra of “ σ^+ out” and “ σ^- out” detection, respectively (note that all the measurements are performed using “ σ^+ in” excitation) [23]. The estimated “ X_0 DOP” percentage as a function of magnetic fields for all studied samples is shown in Figure 4(a). In the case of 1L W^NS₂, “ X_0 DOP” changes from 4% to -30%, with the field increasing from 0 to 14 T, while for pure sulfur isotopes of modified W³²S₂ and W³⁴S₂, the DOP changes from 3% to 0% and 7% to -2%, respectively. Furthermore, Figure 4(b) and (c) displays the calculated “ X_T^- DOP” and “ X_S^- DOP” as a function of a magnetic field. It is observed that “ X_T^- DOP” for 1L W^NS₂ initially increases from 35% to 53% as the field varies from 0 to 5 T and then saturates at higher fields. However, for pure isotope-modified W³²S₂, “ X_T^- DOP” changes from 3% to 51%, and interestingly, for W³⁴S₂, it changes from 0% to -27% with a field varying from 0 to 14 T. “ X_S^- DOP” for W^NS₂ initially rises from 32% to 55% with a field varying from 0 to 5 T and then saturates at higher fields. However, for pure isotopes, W³²S₂ and W³⁴S₂, “ X_S^- DOP” varies from 17% to 8% and 31% to 4%, respectively, as the field changes from 0 to 14 T. Figure 4(d) shows “ LX_1 DOP” for all samples as a function of the applied magnetic field. In this evaluation, we observed that for 1L W^NS₂, “ LX_1 DOP” initially increases from 27% to 48% as the field increases from 0 to 5 T, and thereafter it saturates at higher fields. For the pure S isotope-modified 1Ls W³²S₂ and W³⁴S₂, the DOP is increased from 12% to 28% and from 11% to 24%, respectively, as the magnetic field increases from 0 to 14 T. Notably, “ LX_1 DOP” demonstrates a rapid increase initially with the application of the field (0 → 1 T), followed by a slower rate of increase. “ LX_2 DOP” for W³²S₂ and W³⁴S₂ changes from 19% to 58% and 32% to 43%, respectively, with the field ranging from 0 to 14 T (see SI Figure S7). Conversely, “ XX_0 DOP” changes very minimally with the applied fields (see SI Figure S7). The observed changes of the DOP with the magnetic field can be attributed to interband/interband scattering mechanisms, whose influence has been quantified through the analysis of intensity ratios. Further elucidation on this matter is provided in the next section.

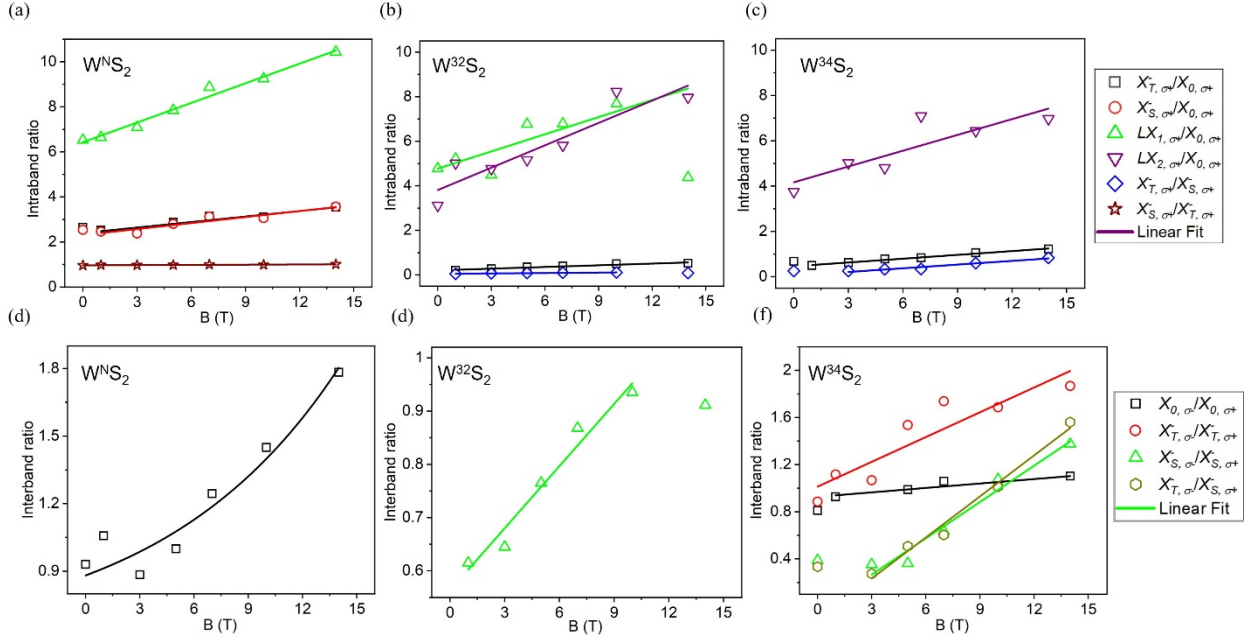


Figure 5. Integral intensity ratios of the highly probable band scattering of quasiparticles under magnetic field ranging from 0 to 14 T at 4 K: (a–c) Intraband ratios and (d–f) interband ratios for $W^N S_2$, $W^{32} S_2$, and $W^{34} S_2$, respectively. Favorable conditions for quasiparticle scattering are indicated by positive slopes of the ratios shown in panels (a) to (f).

Figure 5(a) – (c) shows the intraband intensity ratios estimated between different quasiparticles observed in 1L WS_2 spectra across an applied field ranging from 0 to 14 T at 4 K for $W^N S_2$, $W^{32} S_2$, and $W^{34} S_2$, respectively. The integral intensity values are derived from resonance PL spectra (as shown in Figure 3 and Figure S3(a) in the SI), capturing PL emission and absorption solely from the transitions within the K^+ valley. Earlier studies have indicated that the applied magnetic field can induce alterations in the nature and density of quasiparticles, such as intraband ($K^+ \leftrightarrow K^+$) and interband ($K^+ \leftrightarrow K^-$) scattering, for example, between $X_0 \leftrightarrow X_T^-$ or $X_0 \leftrightarrow LX_1$ [32,57]. The scattering efficiency/probability can be determined by relative intensity ratios (like X_T^-/X_0 , X_S^-/X_0 , X_T^-/X_S^- , LX_1/X_0 , etc.), which correlate to the relative amount of emission of quasiparticles with respect to X_0 , X_T^- , X_S^- , and LX_i ($i = 1, 2$) within the K^+ valley. The intraband ratios for 1L $W^N S_2$, $W^{32} S_2$, and $W^{34} S_2$, plotted against a field, have been fitted by a linear function (*here only positive slope ratios are shown*). The positive sign of the slopes (m) determines the explicit scattering mechanism (like

$X_0 \rightarrow X_T^-$, $X_0 \rightarrow LX_I$, etc.), while a slope of zero indicates the absence of changeable phenomena [26].

Figure 5(d) –(f) illustrates the interband quasiparticle peak intensity ratios for 1L $W^N S_2$, $W^{32} S_2$, and $W^{34} S_2$, respectively, under applied magnetic fields at 4 K. These intensity ratio values are determined from resonance PL spectra, as depicted in Figure 3 and Figure S3(b) in the SI, acquiring the absorption from the K^- valley. Notably, in Figure 5(d), it is demonstrated that the interband intensity ratio of 1L $W^N S_2$ (or the mixed state) exhibits an exponential variation with the applied field, whereas 1L $W^{32} S_2$ and $W^{34} S_2$ show a linear change. This proves that the hyperfine interaction induced by the transition metal is not solely responsible for variation in valley scattering; phonon dispersion induced by sulfur isotope precursors can also provoke substantial platforms for intraband and interband scattering, contrary to a previous report [29]. Consequently, changes in S isotopes lead to variations in phonon dispersion, which refers to how the energy and momentum of phonon modes relate to each other [39,58–60]. This alteration affects the phonon spectrum (see Figure 2(b) and Figure S1), influencing the intra- and inter-valley scattering behavior. The fitted slopes for all possible intraband and interband ratios are detailed in Table S3 (SI).

Intraband and Zeeman Splitting

Further, we have estimated the intraband (band splitting in the K^+ valley) and Zeeman splitting (relative splitting between the K^+ and K^- valleys) of 1L $W^N S_2$, $W^{32} S_2$, and $W^{34} S_2$ (see Figure S8). The intraband shifting of trions with respect to excitons indicates a blueshift for the pure S isotope 1Ls $W^{32} S_2$ and $W^{34} S_2$, while the isotopically mixed sample ($W^N S_2$) exhibits a redshift as the magnetic field increases from 1 to 14 T. In the case of 1L $W^N S_2$, this discrepancy can be observed due to increased disorder in $W^N S_2$ and a higher density of defects in the layer lattice compared to pure isotope samples (1L $W^{32} S_2$ and $W^{34} S_2$.) The presence of disorder induced by isotopic mixing in the mixed-isotope $W^N S_2$ system can significantly impact various factors, including the electronic structure, hyperfine interactions [29], and phonon dispersion [39,59]. These disruptions exacerbate differences in exciton and trion state behavior under a magnetic field, ultimately leading to the observed contrasting spectral shifts [46,61]. Furthermore, the extent of Zeeman splitting in the applied magnetic field corresponds to the value of the g-factor. The valley quasiparticle (X_0 , $X_{i=T,S}^-$, etc.) Zeeman splitting, which is the difference between the quasiparticle transition energies in the K^+ and K^- valleys, is defined as $\Delta E \equiv E(K^+) - (K^-) = -g\mu_B B$, where g denotes the g -

factor of the corresponding excitonic complex and μ_B is the Bohr magneton. In the case of the 1L $W^N S_2$ exciton, it is reported that the splitting is dominated by the atomic orbital moment of the top valence band at the K^+ and K^- valleys, whose g -factor is ≈ 4 [33,62,63]. The g -factor of a negatively charged trion varies from 3 to 5, which was explained by the combined contributions of the spin alignment, the Berry curvature, and the atomic orbital moment [62,63]. However, in the present case, the obtained absolute values of the g -factor for the exciton are 4, 2.3, and 1.7, while for trions, the g -factor values are found to be 3.06, 10, and 2.91 for the 1Ls of $W^N S_2$, $W^{32} S_2$, and $W^{34} S_2$, respectively. (The full list of quasiparticle g -factors is shown in the SI in Table S5.) The g -factor values of excitons and trions for $W^N S_2$ are matched with the reported values [33,63,64]. However, there are no reports for the g -factor values of $W^{32} S_2$ and $W^{34} S_2$. The variation in the g -factor among these samples may stem from reduced atomic orbital magnetic moments as the mass of pure S isotopes increases, alongside alterations in the Berry curvature distribution. The Berry curvature notably impacts phonon dispersion differently across isotopes, influencing the vibrational mode topology and thereby leading to anomalous phonon transport phenomena in the materials [65]. Moreover, for localized excitons exhibiting significant splitting or large g -factors, the underlying mechanisms remain unclear [34]. All fitted slopes for the relative difference between intraband and estimated quasiparticle g -factors are listed in Tables S4 and S5, respectively, in the SI.

Valley Scattering and Upconversion: A Phenomenological Approach

We propose a phenomenological model, as shown in Figure 6, to explain the resonance PL observed in Figure 3 and Figure S3 and the variation in its DOP with an applied magnetic field at 4 K (Figure 4), for the 1Ls of $W^N S_2$, $W^{32} S_2$, and $W^{34} S_2$. The model is based on the results obtained from optical gain (Figure 3(d)) and intensity ratio analysis (Figure 5). The resonance magneto-PL can be described by the two-step process: the first step involves upconversion phenomena due to resonance excitation without a magnetic field, and the second step involves intraband/interband scattering in the K^+ and K^- valleys upon the application of a magnetic field [12,32]. The valleys in 1L TMD are highly sensitive to magnetic fields and light polarization properties [32,57,66,67]. The below-described model is developed for applied fields ($B > 0$) and resonance excitation under light conditions of “ σ^+ in.”

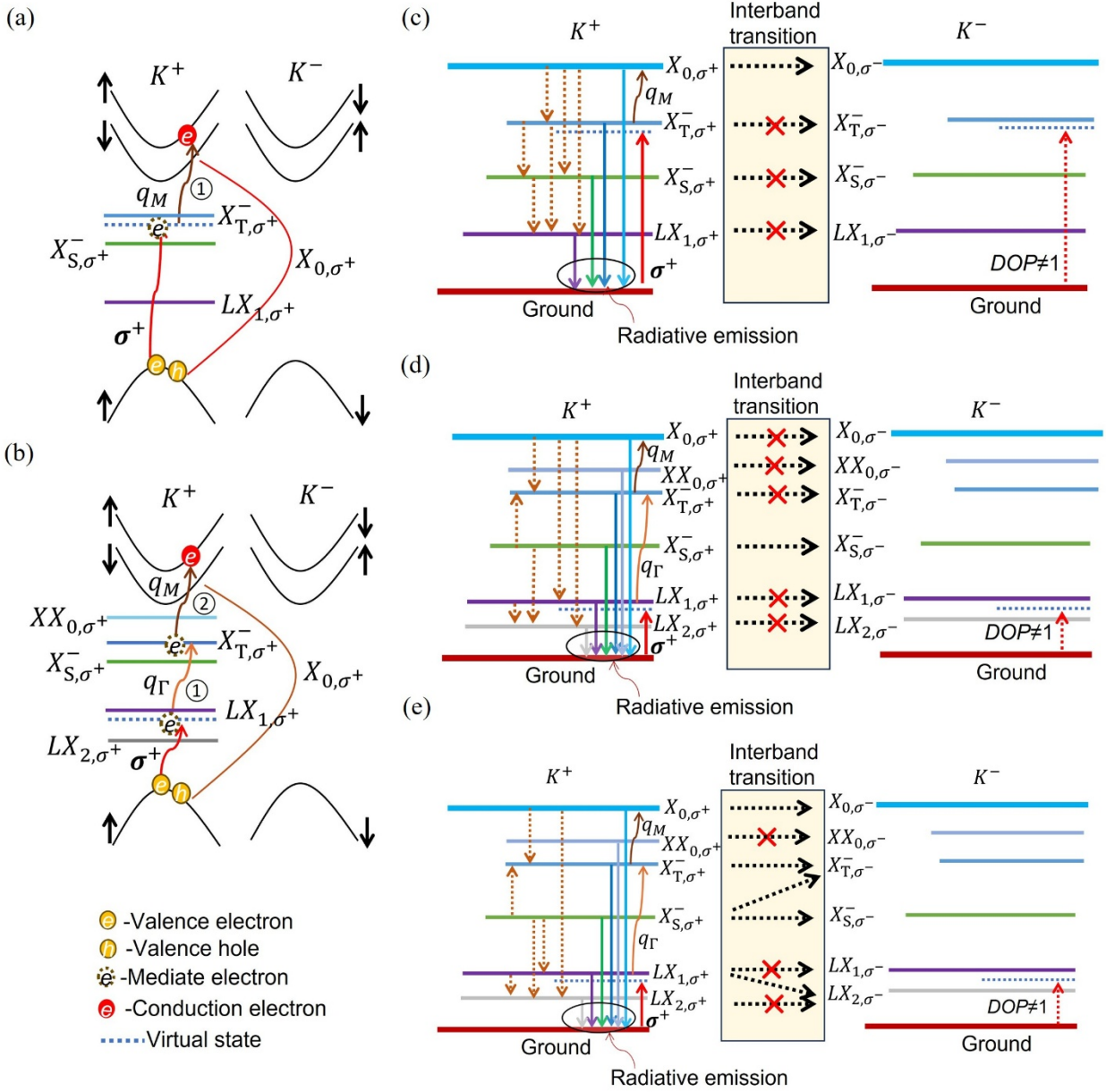


Figure 6. Phenomenological model for resonance magneto-PL of S isotope-modified 1L WS_2 at 4 K: (a) and (b) Distinct energy band diagrams for 1Ls of mixed ($W^N S_2$) and pure sulfurs ($W^{32}S_2$ and $W^{34}S_2$) at 4 K without a magnetic field, respectively. For 1L $W^N S_2$, the energy band consists of quasi-levels of excitons, trions, and one localized exciton, while for 1L $W^{32}S_2$ and $W^{34}S_2$, two additional quasi-levels form: biexcitons and one localized exciton. In the case of $W^N S_2$, one M -phonon is required, while $W^{32}S_2$ and $W^{34}S_2$ require two phonons (M and Γ) for upconversion. (c–e) A comprehensive graphical demonstration of the aforementioned quasi-levels, accompanied by K^+ and K^- valleys under resonant σ^+ excitation for the 1Ls $W^N S_2$, $W^{32}S_2$, and $W^{34}S_2$, respectively,

depicting the intraband (within K^+) and interband (between K^+ and K^-) scattering. The quasiparticle levels for the exciton, biexciton, triplet and singlet trions, and localized exciton on the K^+ valley are represented as X_{0,σ^+} , XX_{0,σ^+} , X_{T,σ^+}^- , X_{S,σ^+}^- , and LX_{i,σ^+} , respectively. The radiative emission to the ground state is indicated by a solid arrow, while possible allowed intraband and interband scattering is represented by light brown and black dotted arrows, respectively. The forbidden interband scattering is marked with a red cross.

Upconversion phenomena

Upconversion phenomena have been previously studied for 1L $W^N S_2$ under resonance excitation at RT (room temperature), as well as cryogenic temperatures [5,12,13]. However, the occurrence of intraband and interband scattering upon the application of a magnetic field under resonance-polarized PL is not yet fully understood. However, Ma et al. [32] described both intra-valley and inter-valley scattering phenomena by solving the rate equations that describe the valley dynamics for non-resonant magneto-optical properties of excitons and trions in a 1L WSe_2 . We exploit these two phenomena to discuss the variation of the quasiparticle DOP under magnetic fields.

The upconversion phenomenon occurred differently in the mixed isotopically modified 1L ($W^N S_2$) and pure S isotope-modified 1Ls ($W^{32} S_2$ and $W^{34} S_2$), as shown in Figure 6(a) and (b), respectively. The identification of intermediate energy bands/levels that trigger the upconversion process is essential in order to understand the underlying mechanism [12,13]. The position of the upconversion intermediate state can be obtained through an optical gain analysis. For $W^N S_2$, the estimated gain is ~ 30 meV (close to the triplet trion peak), while in the case of $W^{32} S_2$ and $W^{34} S_2$, the estimated gain is ~ 80 meV (close to the first localized exciton peak); it is nearly constant with an applied magnetic field (see Figure 3(d)). Further, Figure 6(a) elaborates on the upconversion process of 1L $W^N S_2$; upon the excitation of resonant light, the valence band (VB) electron at the K^+ valley transits to an intermediate virtual state, closely resembling the real trion state (X_T^-). From this trion state, the mediating electron (from the VB) absorbs the M -phonon ($q_M \sim 213 \text{ cm}^{-1}$ or 27 meV, refer to Figure S1(a) in the SI) and scatters to the conduction band (CB) in the same valley [68]. The CB electron exhibits strong coupling with the VB hole, eventually leading to the emission of an exciton (~ 1.989 eV) with an energy greater than the excitation energy. Figure 6(b) exhibits the upconversion process for the pure isotope 1Ls $W^{32} S_2$ and $W^{34} S_2$. Despite the small variation in composition between $^N S$ and $^{32} S$, the 1Ls of $W^N S_2$ and $W^{32} S_2$ demonstrate unique

upconversion behaviors due to distinct phonon dispersion. In the case of pure isotope 1L samples, the upconversion phenomena are found to be stimulated by two-phonon absorption. The electron in the VB (at the K^+ valley) transits to an intermediate virtual energy level, positioned close to the first LX_I . At this point, the mediating electron first absorbs the Γ -phonon (for $W^{32}S_2$, $q_\Gamma \sim 418 \text{ cm}^{-1}$ or 52 meV , and for $W^{34}S_2$, $q_\Gamma \sim 406 \text{ cm}^{-1}$ or 50 meV ; see Figure 2(b) and Figure S1, respectively), scatters to the X_T^- band (at the K^+ valley), and then further absorbs the M -phonon ($q_M \sim 213 \text{ cm}^{-1}$ or 27 meV (for both types of pure isotope-modified WS_2) [68]; see Figure 2(b) and Figure S1), transiting the mediated electron to the CB. Thereafter, the CB electron couples with the VB hole and emits an exciton with an energy greater than the excitation energy, similar to $W^N S_2$.

Intra/inter-valley scattering phenomena

As mentioned in the previous section, the application of magnetic fields induces quasiparticle intraband/interband scattering and valley splitting. The underlying scattering phenomena for 1L $W^N S_2$ are illustrated in Figure 6(c). The analysis of intensity ratios (see Figure 5 and Table S3) reveals that upon applying a magnetic field, excitons at the K^+ valley (X_{0,σ^+}) predominantly scatter to the K^- valley (X_{0,σ^-}), i.e., interband scattering, which is dominant in $W^N S_2$. Additionally, these excitons also scatter to X_{T,σ^+}^- , X_{S,σ^+}^- , and LX_{1,σ^+} , while a proportion of X_{T,σ^+}^- scatter to X_{S,σ^+}^- within the same K^+ valley, i.e., intraband scattering. Similarly, intraband scattering has been observed from the trion band (X_{T,σ^+}^- and X_{S,σ^+}^-) to LX_{1,σ^+} , although the scattering probabilities are comparatively smaller, as substantiated by smaller values of the slopes of the intensity ratio (see Table S3 in the SI). Figure 6(d) illustrates the intraband scattering phenomenon of 1L $W^{32}S_2$, where X_{0,σ^+} scatters to X_{T,σ^+}^- , LX_{1,σ^+} , and LX_{2,σ^+} . Further, X_{T,σ^+}^- shows no trace of scattering to other quasiparticles; however, traces of scattering are observed from X_{S,σ^+}^- to X_{T,σ^+}^- , LX_{1,σ^+} , LX_{2,σ^+} (intraband), and X_{S,σ^-}^- (interband). The majority of quasiparticles settle down to the localized states. The scattering process for $W^{34}S_2$ is illustrated in Figure 6(e), and we note that X_{0,σ^+} scatters solely to X_{T,σ^+}^- , LX_{1,σ^+} (intraband), and X_{0,σ^-} (interband), while XX_0 traces no scattering among its bands. It is noteworthy that interband scattering occurs from X_{T,σ^+}^- to X_{T,σ^-}^- , whereas X_{S,σ^+}^- exhibits both intraband (X_{S,σ^+}^- to X_{T,σ^+}^- , LX_{1,σ^+} , and LX_{2,σ^+} at the K^+ valley) and interband (X_{S,σ^+}^- to X_{T,σ^-}^- and X_{S,σ^-}^- at the K^- valley) scattering. Interestingly, 1L $W^{34}S_2$ shows LX_{1,σ^+} scattering to LX_{2,σ^+} (intraband) and LX_{2,σ^-} (interband). It should be noted that even though

the upconversion phenomena in the 1Ls $W^{32}S_2$ and $W^{34}S_2$ occur due to two-phonon absorption, the intraband and interband scattering are quite distinct. Next, we discuss the correlation of the DOP with the intraband and interband scattering through the approach of phenomenological models described in this section.

“ X_0 DOP” for 1L $W^N S_2$ decreases as the magnetic field increases (see Figure 4(a)) due to the dominant interband scattering from X_{0,σ^+} to X_{0,σ^-} and fewer intraband scatterings to X_{T,σ^+}^- , X_{S,σ^+}^- , and LX_{1,σ^+} , as shown in Figure 6(c). This can be understood from the definition of the DOP for a particular quasiparticle. If there is comparatively larger scattering of quasiparticles at the K^+ point to other quasi-bands (intra/inter-valley), this will lead to a decreased DOP. Conversely, if the scattering is less predominant, it will result in a higher DOP. Similarly, a minimal decrease in the DOP with the magnetic field for the pure S isotope 1Ls $W^{32}S_2$ and $W^{34}S_2$ is observed. For 1L $W^{32}S_2$, this change is small due to the solely intraband scattering of X_{0,σ^+} to X_{T,σ^+}^- and $LX_{i(i=1,2),\sigma^+}$. However, for $W^{34}S_2$, both intraband scattering and interband scattering, i.e., from X_{0,σ^+} to X_{T,σ^+}^- , LX_{2,σ^+} , and X_{0,σ^-} , contribute to a relatively larger decrease in “ X_0 DOP” with the magnetic field. The probability of intra/inter-valley quasiparticle scattering is estimated from the analysis of the slope of the intensity ratio (see Table S3). As mentioned previously, $W^N S_2$ manifests a distinguished phonon spectra due to isotopic disorder. This disorder can enhance intraband and inter-valley scattering processes and reduce the stability of exciton polarization, leading to a decrease in the DOP with an increasing magnetic field [69]. Pure isotope 1Ls result in more uniform phonon interactions [36]. This uniformity can stabilize the exciton states, resulting in minimal change in the DOP with an increasing magnetic field.

“ X_T^- DOP” for $W^N S_2$ exhibits a significant increase as the magnetic field increases from 0 to 5 T and thereafter saturates at higher field values (see Figure 4(b)). The increase in “ X_T^- DOP” can be attributed to the intraband scattering of X_{0,σ^+} to X_{T,σ^+}^- , as the amount of triplet trions is enhanced. The initial rapid increase in “ X_T^- DOP” for trions in $W^N S_2$ up to 5 T can be attributed to the significant influence of the intraband (or Landau level) splitting, which increases the trion binding energy and enhances polarization [64,70] (see Figure S8(a)). However, beyond 5 T, the binding energy of trions reaches a stable state, where additional magnetic field strength does not significantly affect it. This stabilization leads to a gradual saturation in “ X_T^- DOP,” as the trions

are already highly polarized, and further increases in the magnetic field contribute minimally to additional polarization.

Similarly, the increase in “ X_T^- DOP” for $W^{32}S_2$, with the increase in the magnetic field, can be attributed to the intraband scattering of X_{0,σ^+} and X_{S,σ^+}^- to X_{T,σ^+}^- . In contrast, “ X_T^- DOP” for $W^{34}S_2$ exhibits a decrease, reaching $\sim 27\%$ with an increase in the magnetic field, due to the interband scattering of X_{T,σ^+}^- and X_{S,σ^+}^- to X_{T,σ^-}^- . The increase in “ X_T^- DOP” in $W^{32}S_2$ with an increasing magnetic field can be due to stronger electron-phonon interactions, weaker hyperfine interactions, and efficient scattering mechanisms that help align trion spins. Conversely, the decrease in “ X_T^- DOP” in $W^{34}S_2$ can be attributed to weaker electron-phonon interactions, stronger hyperfine interactions, and more complex scattering mechanisms due to heavier isotopes that disrupt trion spin alignment [29,58,60].

Furthermore, “ X_S^- DOP” for $W^N S_2$ initially increases with an applied field from 1 to 5 T (Figure 4(c)), which can be attributed to the intraband scattering of X_{0,σ^+} and X_{T,σ^+}^- to X_{S,σ^+}^- , but the scattering slows down at higher fields, resulting in a nearly saturated DOP. This follows the same behavior and reasoning as the case of “ X_T^- DOP” for $W^N S_2$. In $W^{32}S_2$, “ X_S^- DOP” decreases with increasing magnetic fields. This is because X_{S,σ^+}^- exhibits intraband scattering to X_{T,σ^+}^- and $LX_{i(i=1,2),\sigma^+}$, as well as interband scattering to X_{S,σ^-}^- (see Figure 6(d)). Similarly, in $W^{34}S_2$, “ X_S^- DOP” decreases with increasing magnetic fields due to intraband scattering from X_{S,σ^+}^- to $LX_{i(i=1,2),\sigma^+}$ and interband scattering to X_{S,σ^-}^- and X_{T,σ^-}^- . This behavior can be understood through the interband and intraband (Zeeman) splitting strength (slope or g -factor), which indicates that singlet trions exhibit strong coupling with the magnetic field (see Figure S8 and Tables S4 and S5). This strong coupling leads to the increased scattering of singlet trions, resulting in a decrease in their “ X_S^- DOP” when a magnetic field is applied [71]. Previously, similar trends of exciton and trion DOPs under fields have been reported for the 1Ls $W^N S_2$ and WSe_2 [33,34,57].

Interestingly, “ XX_0 DOP” is nearly constant under varying magnetic fields (see Figure S7(a)) because XX_0 exhibits neither intraband nor interband scattering for pure isotope-modified WS_2 1Ls. Additionally, in all WS_2 1Ls, a high probability of the intraband scattering of quasiparticles (exciton and trions) to the LX state is observed with an increase in the magnetic field, resulting in the increase of “ LX DOPs.” At low temperatures, LX states in WS_2 are considered stable due to

the strong Coulomb interactions, localized potential wells in the crystal lattice, lower energy configurations, longer lifetimes, and experimental evidence confirming their existence [48,72]. Further, at higher magnetic fields, increased scattering probabilities can affect the contribution and interaction of quasiparticles to stabilize LX states by promoting relaxation into these energetically favorable states.

The differences observed in WS_2 properties between $^N S$ -, ^{32}S -, and ^{34}S -derived samples stem from the combined effects of phonon spectrum variations and isotopic disorder [39,59], highlighting the intricate relationship between these factors in determining the material's characteristics.

4. Conclusions

In summary, we investigated the influence of varying S isotopes in 1L WS_2 on PL emission under resonance excitation, as a function of the temperature, magnetic field, and light polarization. By analyzing the DOP and intensity ratios of PL emission corresponding to different excitonic transitions, we observed distinct variations among WS_2 1Ls composed of different S isotopes. Our analysis of intensity ratios and intra/interband (Zeeman) splitting led to a proposed phenomenological model involving intraband/interband scattering and upconversion processes. Notably, upconversion in 1L WS_2 with natural S isotopic abundance involves single-phonon absorption, whereas 1L WS_2 composed of pure ^{32}S and ^{34}S isotopes exhibits two-phonon absorption processes. Moreover, the different S isotopes exhibit unique scattering behaviors: $W^{32}S_2$ shows strong intraband scattering, $W^{34}S_2$ exhibits robust interband scattering, and $W^N S_2$ displays contributions from both. Interband scattering notably results in a more negative DOP, while intraband scattering has the opposite effect. Through intraband scattering processes, quasiparticles are redistributed into localized electronic states, with their degree of localization influenced by the isotope composition. This effect is consistently observed across all isotopic samples, highlighting its fundamental nature. Additionally, the upconversion emission, tunable via isotope variation, enhances the overall light emission efficiency. These findings underscore the potential of S isotope engineering to modulate the properties of 1L TMDs, presenting new opportunities for advancing optoelectronic and photonic devices based on 1L WS_2 .

Acknowledgements:

The work was supported by the Czech Science Foundation, project no. 24-11772S and Ministry of Education, Youth and Sports of the Czech Republic, project QM4ST, no. CZ.02.01.01/00/22_008/0004572.

We also acknowledge the support in the AFM and low-temperature environments provided by the Research Infrastructures NanoEnviCz and MGML, supported by the Ministry of Education, Youth and Sports of the Czech Republic under projects no. LM2015073 and LM2023065, respectively.

5. References

- [1] Choi W, Choudhary N, Han G H, Park J, Akinwande D and Lee Y H 2017 Recent development of two-dimensional transition metal dichalcogenides and their applications *Materials Today* **20** 116–30
- [2] Wang Q H, Kalantar-Zadeh K, Kis A, Coleman J N and Strano M S 2012 Electronics and optoelectronics of two-dimensional transition metal dichalcogenides *Nat Nanotechnol* **7** 699–712
- [3] Kou J, Nguyen E P, Merkoçi A and Guo Z 2020 2-dimensional materials-based electrical/optical platforms for smart on-off diagnostics applications *2d Mater* **7** 32001
- [4] Jones A M, Yu H, Schaibley J R, Yan J, Mandrus D G, Taniguchi T, Watanabe K, Dery H, Yao W and Xu X 2016 Excitonic luminescence upconversion in a two-dimensional semiconductor *Nat Phys* **12** 323–7
- [5] Żuberek E, Majak M, Lubczyński J, Debus J, Watanabe K, Taniguchi T, Ho C H, Bryja L and Jadczyk J 2022 Upconversion photoluminescence excitation reveals exciton–trion and exciton–biexciton coupling in hBN/WS₂/hBN van der Waals heterostructures *Sci Rep* **12** 13699
- [6] De Wild J, Meijerink A, Rath J K, Van Sark W G J H M and Schropp R E I 2011 Upconverter solar cells: Materials and applications *Energy Environ Sci* **4** 4835–48
- [7] Shan S, Huang J, Papadopoulos S, Khelifa R, Taniguchi T, Watanabe K, Wang L and Novotny L 2023 Overbias Photon Emission from Light-Emitting Devices Based on Monolayer Transition Metal Dichalcogenides *Nano Lett* **23** 10908–13
- [8] Lou G, Wu Y, Zhu H, Li J, Chen A, Chen Z, Liang Y, Ren Y, Gui X, Zhong D, Qiu Z, Tang Z and Su S C 2018 Upconversion single-microbelt photodetector via two-photon absorption simultaneous *J Phys D Appl Phys* **51** 19LT01
- [9] Zhang J, Li D, Chen R and Xiong Q 2013 Laser cooling of a semiconductor by 40 kelvin *Nature* **493** 504–8
- [10] Liu G 2015 Advances in the theoretical understanding of photon upconversion in rare-earth activated nanophosphors *Chem. Soc. Rev.* **44** 1635–52

- [11] Jadczyk J, Glazov M, Kutrowska-Girzycka J, Schindler J J, Debus J, Ho C H, Watanabe K, Taniguchi T, Bayer M and Bryja L 2021 Upconversion of Light into Bright Intravalley Excitons via Dark Intervalley Excitons in hBN-Encapsulated WSe₂ Monolayers *ACS Nano* **15** 19165–74
- [12] Jadczyk J, Bryja L, Kutrowska-Girzycka J, Kapuściński P, Bieniek M, Huang Y S and Hawrylak P 2019 Room temperature multi-phonon upconversion photoluminescence in monolayer semiconductor WS₂ *Nat Commun* **10** 107
- [13] Wang Q and Wee A T S 2021 Photoluminescence upconversion of 2D materials and applications *Journal of Physics Condensed Matter* **33** 223001
- [14] Bao D, Del Águila A G, Thu Ha Do T, Liu S, Pei J and Xiong Q 2020 Probing momentum-indirect excitons by near-resonance photoluminescence excitation spectroscopy in WS₂ monolayer *2d Mater* **7** 031002
- [15] Jakubczyk T, Nogajewski K, Molas M R, Bartos M, Langbein W, Potemski M and Kasprzak J 2018 Impact of environment on dynamics of exciton complexes in a WS₂ monolayer *2d Mater* **5** 31007
- [16] Zhou J, Liu Z and Li F 2012 Upconversion nanophosphors for small-animal imaging *Chem Soc Rev* **41** 1323–49
- [17] Sedlmeier A, Achatz D E, Fischer L H, Gorris H H and Wolfbeis O S 2012 Photon upconverting nanoparticles for luminescent sensing of temperature *Nanoscale* **4** 7090–6
- [18] Xiao J, Ye Z, Wang Y, Zhu H, Wang Y and Zhang X 2015 Nonlinear optical selection rule based on valley-exciton locking in monolayer WS₂ *Light Sci Appl* **4** e366
- [19] Wen X, Gong Z and Li D 2019 Nonlinear optics of two-dimensional transition metal dichalcogenides *InfoMat* **1** 317–37
- [20] Torres-Torres C, Perea-López N, Elías A L, Gutiérrez H R, Cullen D A, Berkdemir A, López-Urías F, Terrones H and Terrones M 2016 Third order nonlinear optical response exhibited by mono- and few-layers of WS₂ *2d Mater* **3** 21005
- [21] Yu Y, Turkowski V, Hachtel J A, Poretzky A A, Ievlev A V, Din N U, Harris S B, Iyer V, Rouleau C M, Rahman T S, Geohegan D B and Xiao K 2024 Anomalous isotope effect on

- the optical bandgap in a monolayer transition metal dichalcogenide semiconductor *Sci Adv* **10** eadj0758
- [22] Shan J, Li J, Chu X, Xu M, Jin F, Fang X, Wei Z and Wang X 2018 Enhanced photoresponse characteristics of transistors using CVD-grown MoS₂/WS₂ heterostructures *Appl Surf Sci* **443** 31–8
- [23] Feng S, Cong C, Konabe S, Zhang J, Shang J, Chen Y, Zou C, Cao B, Wu L, Peimyoo N, Zhang B and Yu T 2019 Engineering Valley Polarization of Monolayer WS₂: A Physical Doping Approach *Small* **15** 1805503
- [24] Guo S, Wang Y, Wang C, Tang Z and Zhang J 2017 Large spin-orbit splitting in the conduction band of halogen (F, Cl, Br, and I) doped monolayer WS₂ with spin-orbit coupling *Phys Rev B* **96** 245305
- [25] Sasaki S, Kobayashi Y, Liu Z, Suenaga K, Maniwa Y, Miyauchi Y and Miyata Y 2016 Growth and optical properties of Nb-doped WS₂ monolayers *Applied Physics Express* **9** 071201
- [26] Kesarwani R, Simbulan K B, Huang T-D, Chiang Y-F, Yeh N-C, Lan Y-W and Lu T-H 2022 Control of trion-to-exciton conversion in monolayer WS₂ by orbital angular momentum of light *Sci. Adv* **8** 100
- [27] Trovatello C, Piccinini G, Forti S, Fabbri F, Rossi A, De Silvestri S, Coletti C, Cerullo G and Dal Conte S 2022 Ultrafast hot carrier transfer in WS₂/graphene large area heterostructures *NPJ 2D Mater Appl* **6** 24
- [28] Cunningham P D, Hanbicki A T, McCreary K M and Jonker B T 2017 Photoinduced Bandgap Renormalization and Exciton Binding Energy Reduction in WS₂ *ACS Nano* **11** 12601–8
- [29] Wu Y, Tong Q, Liu G Bin, Yu H and Yao W 2016 Spin-valley qubit in nanostructures of monolayer semiconductors: Optical control and hyperfine interaction *Phys Rev B* **93** 045313
- [30] Vuong T Q P, Liu S, Van der Lee A, Cuscó R, Artús L, Michel T, Valvin P, Edgar J H, Cassabois G and Gil B 2018 Isotope engineering of van der Waals interactions in hexagonal boron nitride *Nat Mater* **17** 152–8

- [31] Varade V, Haider G, Pirker L, Panda J, Sykora J, Frank O, Kalbac M and Vejpravova J 2023 Sulfur isotope engineering of exciton and lattice dynamics in MoS₂ monolayers *2d Mater* **10** 025024
- [32] Ma Y, Wang Q, Han S, Qu F and Fu J 2021 Fine structure mediated magnetic response of trion valley polarization in monolayer WSe₂ *Phys Rev B* **104** 195424
- [33] Plechinger G, Nagler P, Arora A, Granados Del Águila A, Ballottin M V., Frank T, Steinleitner P, Gmitra M, Fabian J, Christianen P C M, Bratschitsch R, Schüller C and Korn T 2016 Excitonic Valley Effects in Monolayer WS₂ under High Magnetic Fields *Nano Lett* **16** 7899–904
- [34] Koperski M, Molas M R, Arora A, Nogajewski K, Bartos M, Wyzula J, Vaclavkova D, Kossacki P and Potemski M 2019 Orbital, spin and valley contributions to Zeeman splitting of excitonic resonances in MoSe₂, WSe₂ and WS₂ Monolayers *2d Mater* **6** 015001
- [35] Rodriguez-Nieva J F, Saito R, Costa S D and Dresselhaus M S 2012 Effect of ¹³C isotope doping on the optical phonon modes in graphene: Localization and Raman spectroscopy *Phys Rev B Condens Matter Mater Phys* **85** 245406
- [36] Cardona M and Thewalt M L W 2005 Isotope effects on the optical spectra of semiconductors *Rev Mod Phys* **77** 1173–224
- [37] Li X, Zhang J, Puretzy A A, Yoshimura A, Sang X, Cui Q, Li Y, Liang L, Ghosh A W, Zhao H, Unocic R R, Meunier V, Rouleau C M, Sumpter B G, Geohegan D B and Xiao K 2019 Isotope-engineering the thermal conductivity of two-dimensional MoS₂ *ACS Nano* **13** 2481–9
- [38] Cuscó R, Edgar J H, Liu S, Li J and Artús L 2020 Isotopic Disorder: The Prevailing Mechanism in Limiting the Phonon Lifetime in Hexagonal BN *Phys Rev Lett* **124** 167402
- [39] Wu W, Morales-Acosta M D, Wang Y and Pettes M T 2019 Isotope Effect in Bilayer WSe₂ *Nano Lett* **19** 1527–33
- [40] Islam M S, Ushida K, Tanaka S and Hashimoto A 2013 Numerical experiments on phonon properties of isotope and vacancy-type disordered graphene *Diam Relat Mater* **40** 115–22

- [41] Varade V, Haider G, Slobodeniuk A, Korytar R, Novotny T, Holy V, Miksatko J, Plsek J, Sykora J, Basova M, Zacek M, Hof M, Kalbac M and Vejpravova J 2023 Chiral Light Emission from a Hybrid Magnetic Molecule-Monolayer Transition Metal Dichalcogenide Heterostructure *ACS Nano* **17** 2170–81
- [42] Shang H, Zhao J and Yang J 2021 Assessment of the Mass Factor for the Electron–Phonon Coupling in Solids *The Journal of Physical Chemistry C* **125** 6479–85
- [43] Molas M R, Nogajewski K, Potemski M and Babiński A 2017 Raman scattering excitation spectroscopy of monolayer WS₂ *Sci Rep* **7** 5036
- [44] Plekhanov V G and Plekhanov N V 2003 Isotope dependence of band-gap energy *Phys Lett A* **313** 231–7
- [45] Jadczyk J, Kutrowska-Girzycka J, Kapuściński P, Huang Y S, Wójs A and Bryja L 2017 Probing of free and localized excitons and trions in atomically thin WSe₂, WS₂, MoSe₂ and MoS₂ in photoluminescence and reflectivity experiments *Nanotechnology* **28** 395702
- [46] Plechinger G, Nagler P, Arora A, Schmidt R, Chernikov A, del Águila A G, Christianen P C M, Bratschitsch R, Schüller C and Korn T 2016 Trion fine structure and coupled spin–valley dynamics in monolayer tungsten disulfide *Nat Commun* **7** 12715
- [47] Vaclavkova D, Wyzula J, Nogajewski K, Bartos M, Slobodeniuk A O, Faugeras C, Potemski M and Molas M R 2018 Singlet and triplet trions in WS₂ monolayer encapsulated in hexagonal boron nitride *Nanotechnology* **29** 325705
- [48] Hichri A, Amara I Ben, Ayari S and Jaziri S 2017 Dielectric environment and/or random disorder effects on free, charged and localized excitonic states in monolayer WS₂ *Journal of Physics Condensed Matter* **29** 435305
- [49] Naik M H and Jain M 2018 Substrate screening effects on the quasiparticle band gap and defect charge transition levels in MoS₂ *Phys Rev Mater* **2** 84002
- [50] Upadhyay B, Thakur D, Pramanick B, Bhandari S, Balakrishnan V and Pal S K 2022 Anomalous emission behavior of excitons at low temperature in monolayer WS₂ *J Phys D Appl Phys* **55** 235105

- [51] Wei K, Liu Y, Yang H, Cheng X and Jiang T 2016 Large range modification of exciton species in monolayer WS₂. *Appl Opt* **55** **23** 6251–5
- [52] Molas M R, Nogajewski K, Slobodeniuk A O, Binder J, Bartos M and Potemski M 2017 The optical response of monolayer, few-layer and bulk tungsten disulfide *Nanoscale* **9** 13128–41
- [53] Pierret A, Tornatzky H and Maultzsch J 2019 Anti-Stokes Photoluminescence of Monolayer WS₂ *physica status solidi (b)* **256** 1900419
- [54] Golovynskiy S, Datsenko O I, Dong D, Lin Y, Irfan I, Li B, Lin D and Qu J 2021 Trion Binding Energy Variation on Photoluminescence Excitation Energy and Power during Direct to Indirect Bandgap Crossover in Monolayer and Few-Layer MoS₂ *The Journal of Physical Chemistry C* **125** 17806–19
- [55] Li H, Ma Y, Sui Y, Tang Y, Wei K, Cheng X and Jiang T 2020 Valley depolarization in downconversion and upconversion emission of monolayer WS₂ at room temperature *Nanophotonics* **9** 4809–18
- [56] Wang G, Chernikov A, Glazov M M, Heinz T F, Marie X, Amand T and Urbaszek B 2018 Colloquium: Excitons in atomically thin transition metal dichalcogenides *Rev Mod Phys* **90** 21001
- [57] Aivazian G, Gong Z, Jones A M, Chu R L, Yan J, Mandrus D G, Zhang C, Cobden D, Yao W and Xu X 2015 Magnetic control of valley pseudospin in monolayer WSe₂ *Nat Phys* **11** 148–52
- [58] Cardona M and Thewalt M L W 2005 Isotope effects on the optical spectra of semiconductors *Rev Mod Phys* **77** 1173–224
- [59] Tamura S 1983 Isotope scattering of dispersive phonons in Ge *Phys Rev B* **27** 858–66
- [60] Haller E E 1995 Isotopically engineered semiconductors *J Appl Phys* **77** 2857–78
- [61] Ochoa H and Roldán R 2013 Spin-orbit-mediated spin relaxation in monolayer MoS₂ *Phys Rev B* **87** 245421

- [62] Cong C, Zou C, Cao B, Wu L, Shang J, Wang H, Qiu Z, Hu L, Tian P, Liu R and Yu T 2018 Intrinsic excitonic emission and valley Zeeman splitting in epitaxial MS_2 ($M = Mo$ and W) monolayers on hexagonal boron nitride *Nano Res* **11** 6227–36
- [63] Kapuściński P, Vaclavkova D, Grzeszczyk M, Slobodeniuk A O, Nogajewski K, Bartos M, Watanabe K, Taniguchi T, Faugeras C, Babiński A, Potemski M and Molas M R 2020 Valley polarization of singlet and triplet trions in a WS_2 monolayer in magnetic fields *Phys. Chem. Chem. Phys.* **22** 19155–61
- [64] Lyons T P, Dufferwiel S, Brooks M, Withers F, Taniguchi T, Watanabe K, Novoselov K S, Burkard G and Tartakovskii A I 2019 The valley Zeeman effect in inter- and intra-valley trions in monolayer WSe_2 *Nat Commun* **10** 2330
- [65] Liu Y, Chen X and Xu Y 2020 Topological Phononics: From Fundamental Models to Real Materials *Adv Funct Mater* **30** 1904784
- [66] Rong R, Liu Y, Nie X, Zhang W, Zhang Z, Liu Y and Guo W 2023 The Interaction of 2D Materials With Circularly Polarized Light *Advanced Science* **10** 2206191
- [67] Li Z, Wang T, Miao S, Lian Z and Shi S F 2020 Fine structures of valley-polarized excitonic states in monolayer transitional metal dichalcogenides *Nanophotonics* **9** 1811–29
- [68] Berkdemir A, Gutiérrez H R, Botello-Méndez A R, Perea-López N, Elías A L, Chia C-I, Wang B, Crespi V H, López-Urías F, Charlier J-C, Terrones H and Terrones M 2013 Identification of individual and few layers of WS_2 using Raman Spectroscopy *Sci Rep* **3** 1755
- [69] Yu T and Wu M W 2016 Valley depolarization dynamics and valley Hall effect of excitons in monolayer and bilayer MoS_2 *Phys Rev B* **93** 45414
- [70] Adhikary S, Mohakud S and Dutta S 2023 Valley polarization and stable triplet exciton formation in two-dimensional lateral heterostructure of kagome kagome h -BN and graphene *Phys Rev B* **108** 195429
- [71] Schmidt R, Arora A, Plechinger G, Nagler P, Granados del Águila A, Ballottin M V, Christianen P C M, Michaelis de Vasconcellos S, Schüller C, Korn T and Bratschitsch R 2016 Magnetic-Field-Induced Rotation of Polarized Light Emission from Monolayer WS_2 *Phys Rev Lett* **117** 77402

- [72] Ayari S, Smiri A, Hichri A, Jaziri S and Amand T 2018 Radiative lifetime of localized excitons in transition-metal dichalcogenides *Phys Rev B* **98** 205430